A Range Image Processing Approach for Orthodontic Diagnosis

D. Laurendeau, R. Wolfe, M. Mokhtari, L. Guimond
Computer Vision and Systems Laboratory, Department of Electrical and Computer Engineering
Laval University, Ste-Foy, (Que), Canada, G1K 7P4
[laurend,wolfe,marielle,lguimond]@gel.ulaval.ca
http://www.gel.ulaval.ca/~vision

Abstract

This paper presents the latest developments in the design of a computer vision-based system for automatic diagnosis in orthodontics. The need for an automatic diagnosis system in orthodontics is first discussed. The principal components of the system are then introduced and the strategy for the acquisition of range information on the shape of the mandibular and maxillary arches is presented. This is followed by a description of the range acquisition approach used to acquire registered 2D and 3D images of the arches. Since the acquisition has been described in detail elsewhere, this paper focuses on the algorithm for the removal of interreflection to improve the accuracy in range. The algorithms for processing the image data leading to the measurement of a set of orthodontic parameters are described and experimental results are presented showing the performance of the system on a large set of data.

1. The need for an automatic diagnosis system for orthodontics

The purpose of orthodontics is to evaluate the quality of occlusion between the teeth of the mandibular arch and those on the maxillary arch. Once the quality of the occlusion has been evaluated, an orthodontist or even an expert system can decide whether the patient needs dental work or not. Considering the cost of dental care, there is an urgent need for an automatic diagnosis system for conducting epidemiological studies or for screening health insurance beneficiaries.

Several approaches have been proposed to estimate the quality of occlusion [1]. Among these approaches, the measurement of a set of 10 orthodontic parameters has proven to be both practical and efficient [2]. Each parameter describes the relation between specific points located on the teeth. For instance, the cusps on the molars and the premolars, the apex on the canine, and the cutting edge of the incisors are among the points or set of points of interest (see Figure 1). The set of parameters is fed to an expert system for diagnosis. The expert system has been trained by highly qualified orthodontists using a large number of samples.

The orthodontic parameters are currently being measured manually by the orthodontist on plaster models of a patient's mouth. This procedure is slow and often brings discomfort to the patient. Furthermore, the models must be altered manually to improve the cast. When the cast is ready for each arch, the orthodontist has to measure the parameters with a caliper by slightly altering the occlusion between the casts of the arches by opening the model (see Figure 2). This perturbation leads to significant estimation errors of the parameter values. A non-contact approach is called for and computer vision is particularly adapted to this application.

Figure 1 View of the right hand side of a mandibular arch showing points of interest for orthodontic diagnosis.

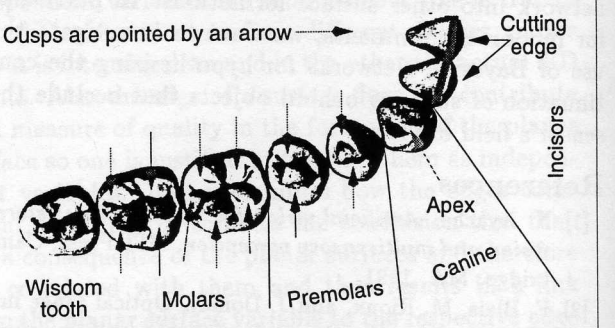

Figure 2 Manual measurement of orthodontic parameters on a plaster cast of the maxillary and mandibular arches.

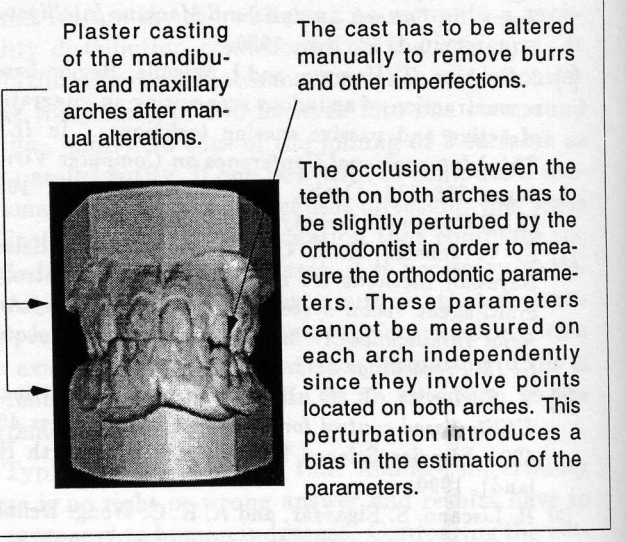

2. Non-contact acquisition of the 3D profile of the arches

An alternative method for recording occlusion is to use a wax bite wafer (see Figure 3) instead of a plaster cast. This recording method is cheaper than the cast approach and is less unpleasant for the patient. Since the imprint is a direct image of occlusion (both arches make contact on each side of the wafer), a proper analysis of its 3D shape can lead to an unbiased and objective estimation of occlusion.

Figure 3 (a) A wax wafer showing the dental imprint of a maxillary arch. (b) The 3D image of the wafer in (a). (c) Enlargment of a molar. (d) Same molar with sensor fusion.

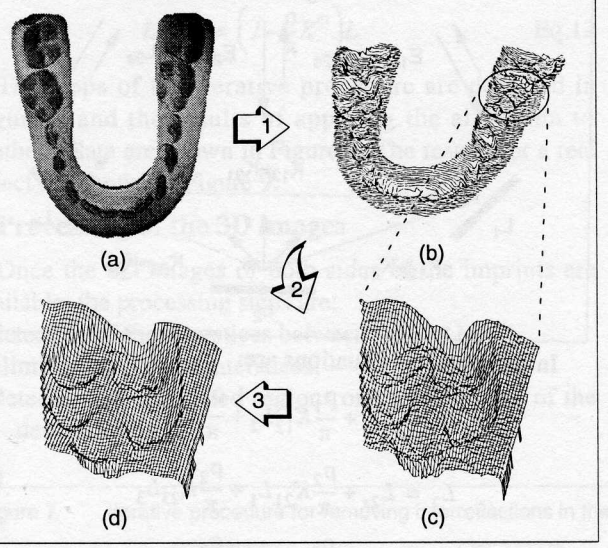

2.1 Range data acquisition process

The 3D image of each side of the wax wafer is obtained using an approach based on the differential absorption of light (DAL) by a diffusing medium. The range acquisition method is described in detail in [11] and is briefly summarized below.

The dental imprint is immersed in a container filled with colored liquid. The absorption spectrum of the liquid shows a peak at 625 nm and is transparent to other wavelengths. A CCD camera is placed on each side of the container and observes one side of the imprint which is illuminated by a lighting system. A first image of the imprint is acquired at a wavelength λ_1 = 600 nm which is absorbed by the liquid. A second image is then taken at a wavelength λ_2 = 750 nm (infrared) which is not absorbed by the liquid. This second image is simply an illuminance image of the imprint and is in perfect registration with the image at λ_1. Range is computed at each pixel using the following equations:

$$dE_{\lambda_1}(i,j) = K_1 \cos(\phi(i,j))\, e^{-2az(i,j)} \qquad \text{Eq.1}$$

$$dE_{\lambda_2}(i,j) = K_2 \cos(\phi(i,j)) \qquad \text{Eq.2}$$

$$z(i,j) = \frac{1}{2\alpha} ln\left[\frac{dE_{\lambda_2}(i,j)}{dE_{\lambda_1}(i,j)}\right] + \frac{1}{2\alpha} ln\left[\frac{K_1}{K_2}\right] \qquad \text{Eq.3}$$

where ϕ is the orientation of the normal to the surface, z is the depth of the point in the liquid and K_1, K_2, and α are parameters obtained through a calibration procedure. Eq.1 and Eq.2 are the illuminance images at λ_1 and λ_2 respectively. Eq.3 is the value of range z at pixel (i,j) computed by dividing $dE_{\lambda_2}(i,j)$ by $dE_{\lambda_1}(i,j)$.

Since Eq.3 involves a division between two illuminance images, the measurement error on range is larger than the noise in each illuminance image. However, it is possible to use sensor fusion to improve the accuracy of range measurements. The 3D image and the illuminance image taken at λ_2 are in perfect registration. A shape-from-shading algorithm is applied to the illuminance image and progressively refines the 3D image through a relaxation technique [10]. The initial 3D image is used as a starting point for the shading algorithm and allows to deal with the concavity/convexity ambiguity. Figure 3 shows the results of the acquisition process.

2.2 Reduction of interreflections

The DAL acquisition method is affected by light interreflected between surface facets in concavities of the measured object. Interreflected light, greater in the infrared image $dE_{\lambda_2}(i,j)$ than in the absorption image $dE_{\lambda_1}(i,j)$, guarantees the over-estimation of ratio $dE_{\lambda_2}(i,j)/dE_{\lambda_1}(i,j)$, and hence, the depth as shown in Figure 4.

Figure 4 Effect of the interreflections on the measurement of a concave 3D shape.

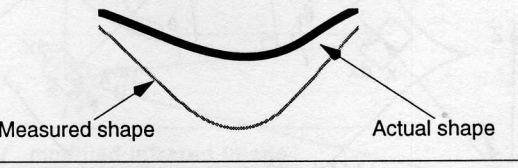

We have designed an algorithm, based on the discretisation of the radiosity equation for Lambertian surfaces, to improve depth estimates by iteratively removing the diffuse (Lambertian) interreflected light component from the intensity images.

The discrete radiosity equation (Eq.4) represents the balance of radiation energy in a digitized scene. In the discrete format, summation replaces integration and indices (i,j) represent pairs of surface facets (pixels) instead of pairs of points. This equation expresses a mathematical basis for separation of directly reflected source light from interreflected light.

$$L_i = L_{si} + \frac{\rho_i}{\pi} \sum_{j \neq i} K_{ij} L_j \qquad \text{Eq.4}$$

with

$$L_{si} = \frac{\rho_i}{\pi} E_{si} \qquad \text{Eq.5}$$

and where

- L_i is the total luminance of each surface facet,
- L_{si} is the luminance due to direct source light,
- ρ_i is the albedo of each facet,
- E_{si} is the illuminance at each facet of direct source light,
- K_{ij} is the interreflection kernel which is the geometric factor for radiation energy transfer between facet pairs [4][5][6][8][9],
- L_j is the luminosity of any other facet.

For a better understanding of the role of the interreflection kernel, we have to consider the two surface elements dx and dx' shown in Figure 5. The goal is to compute the luminance $L(x)$ at x caused by luminance $L(x')$ of x'. This luminance is zero if the two surface elements do not see each other. This occurs when the projection of one of the normal to the surface at these points on the ray joining the two points is negative (e.g. angles θ_i et θ_r must be within the 0 et 90° range for the two surface elements to see each other). This visibility condition can be expressed as:

$$V(x,x') = \frac{n\cdot(-r) + |n\cdot(-r)|}{2|n\cdot(-r)|} \cdot \frac{n'\cdot r + |n'\cdot r|}{2|n'\cdot r|} \qquad \text{Eq.6}$$

This value of the function is 1 when the two surface elements are visible from each other and 0 otherwise.

Figure 5 Concave surface with two patches seeing each other.

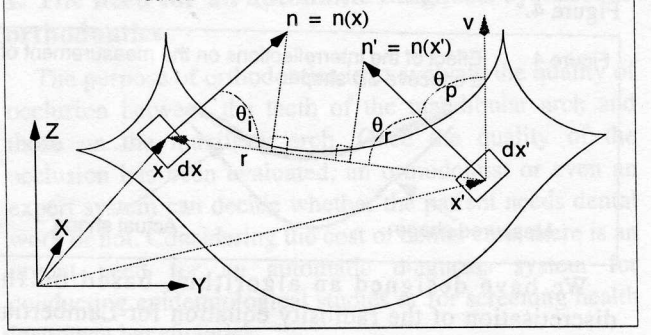

Occlusion is another factor that can affect the visibility between two surface elements. For this purpose, a function $Occ(x,x')$ is defined that produces 0 when two elements are occluded from each other and 1 otherwise. The determination of $Occ(x,x')$ is very complex since it depends on the global geometry of the surface which is unknown *a priori*. We have implemented a parallel algorithm running on a MasPar SIMD machine for the determination of the occlusion function of a regularly sampled surface [12].

The strategy for removing interreflections is to iteratively estimate the luminance at each point using a recursive estimation of the interreflection kernel under the Lambertian assumption. A common approach to this problem is to consider the system as if it were evolving toward an equilibrium state (through a set of equations based on Neumann series [9]). Instead of adopting this line of reasoning, we consider, rather, that the system has reached its equilibrium state. We then take into account the effect of an additional reflection to this equilibrium state. This can be expressed as:

$$L_i = L_{si} + \frac{\rho_i}{\pi} \sum_{j \neq i} K_{ij} L_j \qquad \text{Eq.7}$$

Figure 6 shows a three-facet problem.

Figure 6 Radiosity equation: a three-facet example.

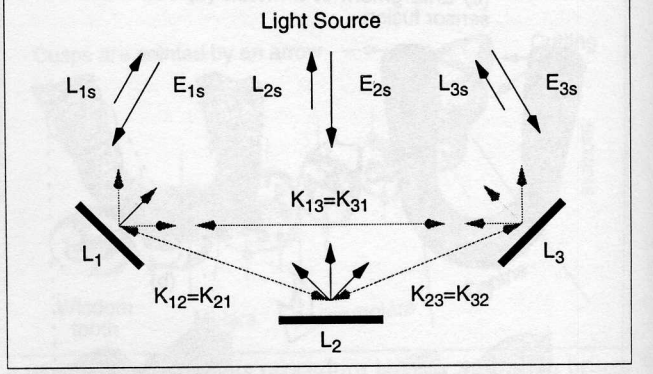

In this case, the equations are:

$$\begin{aligned} L_1 &= L_{1s} + \frac{\rho_1}{\pi} K_{12} L_2 + \frac{\rho_1}{\pi} K_{13} L_3 \\ L_2 &= L_{2s} + \frac{\rho_2}{\pi} K_{21} L_1 + \frac{\rho_2}{\pi} K_{23} L_3 \\ L_3 &= L_{3s} + \frac{\rho_3}{\pi} K_{31} L_1 + \frac{\rho_3}{\pi} K_{32} L_2 \end{aligned} \qquad \text{Eq.8}$$

which can be rearranged as:

$$\begin{bmatrix} L_1 \\ L_2 \\ L_3 \end{bmatrix} = \begin{bmatrix} L_{1s} \\ L_{2s} \\ L_{3s} \end{bmatrix} + \left(\frac{1}{\pi}\right) \begin{bmatrix} \rho_1 & 0 & 0 \\ 0 & \rho_2 & 0 \\ 0 & 0 & \rho_3 \end{bmatrix} \begin{bmatrix} 0 & K_{12} & K_{13} \\ K_{21} & 0 & K_{23} \\ K_{31} & K_{32} & 0 \end{bmatrix} \begin{bmatrix} L_1 \\ L_2 \\ L_3 \end{bmatrix} \qquad \text{Eq.9}$$

and, in a more compact matrix form, as:

$$L = L_s + PKL \qquad \text{Eq.10}$$

The form of Eq.10 allows us to design an iterative algorithm for refining the 3D data acquired with the DAL approach. Assuming that there are no interreflections (the albedo is assumed constant over the whole surface), this means that scene luminance is a result of the light received from the source only (e.g. $L = L_s^1$). Of course, the assumption that there are no interreflections is false, which simply means that L_s^1 is overestimated. Nevertheless, it is still possible to compute a first estimate for K^1 which can be replaced into Eq.10. From this point, the new value for L_s and K can be iteratively computed according to following procedure:

$$
\begin{aligned}
L &= L_s^1 \\
L &= L_s^2 + \frac{\rho}{\pi} K^1 L \\
L &= L_s^3 + \frac{\rho}{\pi} K^2 L \\
&\ldots = \ldots + \ldots \\
L &= L_s^{m+1} + \frac{\rho}{\pi} K^m L
\end{aligned}
\qquad \text{Eq.11}
$$

We expect the value of L_s to decrease and the value of K to increase at each iteration. The algorithm is expected to converge since $(\rho < 1)$. Eq.11 can be written in matrix form as:

$$L_s^{m+1} = \left(I - \frac{\rho}{\pi} K^m\right) L \qquad \text{Eq.12}$$

The steps of the iterative procedure are depicted in Figure 7 and the results of applying the algorithm to synthetic data are shown in Figure 8. The results for a real object are shown in Figure 9.

3. Processing of the 3D images

Once the 3D images of both sides of the imprints are available, the processing steps are:

1•detection of the interstices between present teeth;
2•elimination of false interstices;
3•detection of connected regions on the 3D image of the dental imprint;
4•surface reconstruction of a tooth;
5•detection of feature points on reconstructed images of teeth.

Each processing step is described briefly in the following.

3.1 Detection of the interstices between present teeth

The range images resulting from sensor fusion are

Figure 8 Results of the iterative algorithm for the removal of interreflections on a synthetic 3D object.

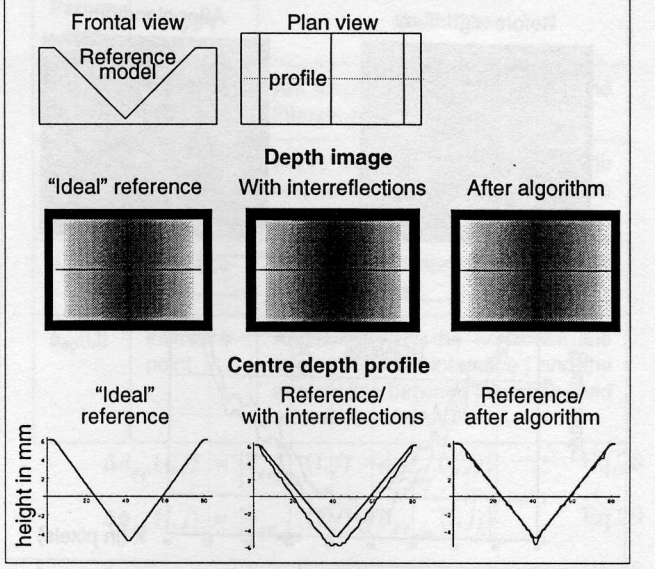

Figure 7 Iterative procedure for removing interreflections in the DAL 3D acquisition system.

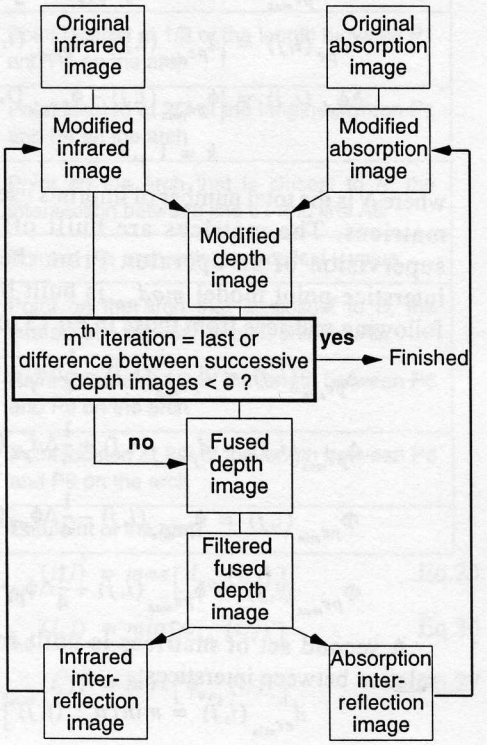

Calculation or extracted factor

L_i

$$L_{si}^{m+1} = L_i - \frac{\rho_i}{\pi} \sum_{j \neq i} K_{ij}^m L_j$$

$$z^m = \beta \ln\left(\frac{\text{modified infrared image}}{\text{modified absorption image}} + \gamma\right) + C$$

β, γ, C = calibration paramaters ; z = depth

2D-3D fusion by relaxation

edge detection
median filtering
hierarchical average filtering

K_{ij}^m

$$\frac{\rho_i}{\pi} \sum_{j \neq i} K_{ij}^m L_j$$

Figure 9 Result of the algorithm for the removal of interreflections on real data (depth image).

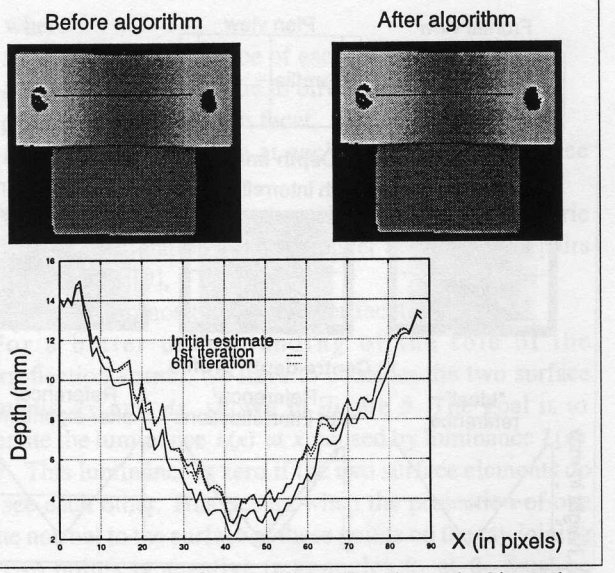

processed to extract the position of each tooth. Since there is no such thing as an ideal arch, it is easier to search for the interstices between the teeth in a first stage, and then to identify the type of tooth from the location of the interstices in a second stage.

In the first stage, the central axis of the imprint is found. A set of operators that yield characteristic 3D curves along the axis is then applied on the 3D image along the axis. The position of the interstices between adjacent teeth are detected from the processing of the output of these operators. Detailed information on the operators can be found in [3]. Figure 10 shows the interstices that were detected on the imprint using these operators.

Figure 10 3D image processing for the identification of the teeth on the image of the imprint.

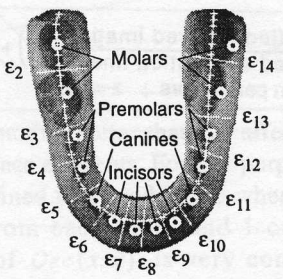

On one hand, it may occur that extraneous interstices appear in the molar or incisor areas because of a poor imprint or because of acquisition noise. On the other hand, interstices may be missing because of a missing tooth or because the operators failed to detect an interstice. To eliminate these false interstices and to take into account the case of missing interstices, we have designed a strategy that is based on the generic structure of a *normal* dentition. It must be pointed out that there is no such thing as an *ideal* dentition in orthodontics. For instance, the dentition varies with the size and race of a person. Consequently, even though it is not possible to define an ideal imprint where the position of each interstice is known very accurately, it still is possible to define a *range* for the position of the interstice relative to a set of *reference* points on the imprint axis. Let us consider the diagram of the normal dentition shown in Figure 11 where *actual* interstices have been numbered ε_1 to ε_{15} and potential *false* interstices have been numbered $-\varepsilon_1$ to $-\varepsilon_{16}$ (see Figure 11a). A set of reference points numbered P_1 to P_9 is defined on the axis of the arch (see Figure 11b). They are chosen in such a way that each one is always located close to the same area of the arch. The definition of each reference point is given in Table 1.

Using the references in Table 1, we define a set of relations between the location of each interstice on the axis and the reference points and between each interstice and the other interstices. The first set of relations consists in the two parameters defined in Figure 11c and the second set of relations is defined in Figure 11d. The meaning of each parameter is summarized in Table 2.Once these parameters are defined, we can build the following set of matrices using a large number of imprints:

$$d_{pe_{min}}(i,j) = min\left[d_{pe_k}(i,j)\right] \quad \text{Eq.13}$$

$$d_{pe_{max}}(i,j) = max\left[d_{pe_k}(i,j)\right] \quad \text{Eq.14}$$

$$\phi_{pe_{min}}(i,j) = min\left[\phi_{pe_k}(i,j)\right] \quad \text{Eq.15}$$

$$\phi_{pe_{max}}(i,j) = max\left[\phi_{pe_k}(i,j)\right] \quad \text{Eq.16}$$

$$\Delta d_{pe}(i,j) = \left|d_{pe_{max}}(i,j) - d_{pe_{min}}(i,j)\right| \quad \text{Eq.17}$$

$$\Delta\phi_{pe}(i,j) = \left|\phi_{pe_{max}}(i,j) - \phi_{pe_{min}}(i,j)\right| \quad \text{Eq.18}$$

$$k = 1 \ldots N \quad \text{Eq.19}$$

where N is the total number of imprints used for building the matrices. The matrices are built off-line under the supervision of an operator. From these matrices the interstice-point model mod_{pe} is built by computing the following matrices from those in Eq.13 to Eq.18:

$$\Delta_{pe_{min}}(i,j) = d_{pe_{min}}(i,j) - \frac{1}{4}\Delta d_{pe}(i,j) \quad \text{Eq.20}$$

$$\Delta_{pe_{max}}(i,j) = d_{pe_{max}}(i,j) + \frac{1}{4}\Delta d_{pe}(i,j) \quad \text{Eq.21}$$

$$\Phi_{pe_{min}}(i,j) = \phi_{pe_{min}}(i,j) - \frac{1}{4}\Delta\phi_{pe}(i,j) \quad \text{Eq.22}$$

$$\Phi_{pe_{max}}(i,j) = \phi_{pe_{max}}(i,j) + \frac{1}{4}\Delta\phi_{pe}(i,j) \quad \text{Eq.23}$$

A second set of matrices is built for expressing the relation between interstices:

$$d_{ee_{min}}(i,j) = min\left[d_{ee_k}(i,j)\right] \quad \text{Eq.24}$$

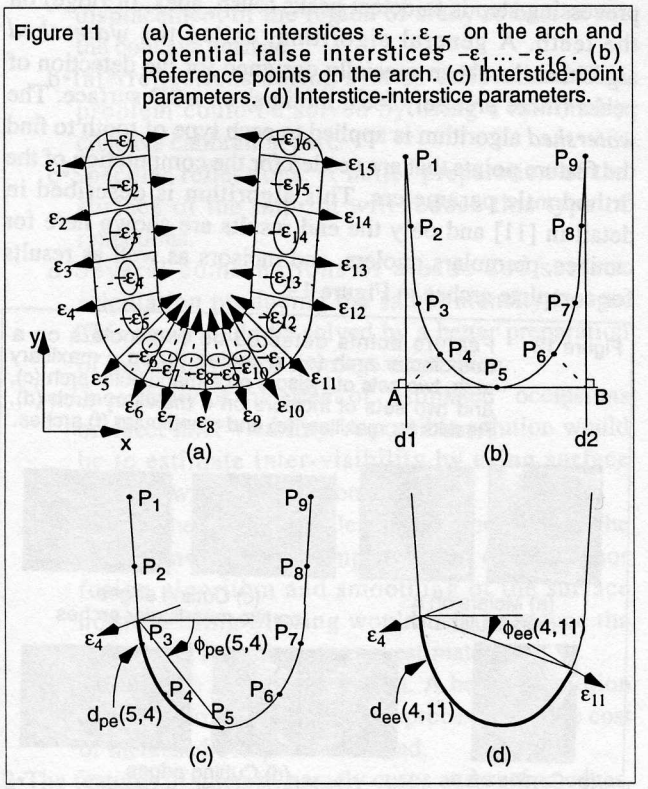

Figure 11 (a) Generic interstices $\varepsilon_1 \ldots \varepsilon_{15}$ on the arch and potential false interstices $-\varepsilon_1 \ldots -\varepsilon_{16}$. (b) Reference points on the arch. (c) Interstice-point parameters. (d) Interstice-interstice parameters.

Table 1 Definition of reference points on the arch

Ref. Point	Definition
P_1	First point on the arch
P_2	Point located at 1/3 of the length between P1 and P4 on the arch
P_3	Point located at 2/3 of the length between P1 and P4 on the arch
P_4	Point on the arch that is closest to A, the intersection between line d1 and line AB
P_5	Point of the arch with the smallest y value
P_6	Point on the arch that is closest to B, the intersection between line d2 and line AB
P_7	Point located at 1/3 of the length between P6 and P9 on the arch
P_8	Point located at 2/3 of the length between P6 and P9 on the arch
P_9	Endpoint of the arch

$$d_{ee_{max}}(i,j) = max\left[d_{ee_k}(i,j)\right] \quad \text{Eq.25}$$

$$\phi_{ee_{min}}(i,j) = min\left[\phi_{ee_k}(i,j)\right] \quad \text{Eq.26}$$

$$\phi_{ee_{max}}(i,j) = max\left[\phi_{ee_k}(i,j)\right] \quad \text{Eq.27}$$

Table 2 Definition of the parameters show in Figure 11c and Figure 11d.

Parameter	Type	Definition
$d_{ee}(i,j)$	interstice-interstice	Arc length between interstice i and interstice j
$\phi_{ee}(i,j)$	interstice-interstice	Angle between the horizontal line originating from interstice i and the straight line between i and j.
$d_{ep}(i,j)$	interstice-point	Arc length between reference point i and interstice j.
$\phi_{ep}(i,j)$	interstice-point	Angle between the horizontal line originating from interstice j and the straight line between interstice j and reference point i.

$$\Delta d_{ee}(i,j) = \left|d_{ee_{max}}(i,j) - d_{ee_{min}}(i,j)\right| \quad \text{Eq.28}$$

$$\Delta \phi_{ee}(i,j) = \left|\phi_{ee_{max}}(i,j) - \phi_{ee_{min}}(i,j)\right| \quad \text{Eq.29}$$

$$k = 1 \ldots N \quad \text{Eq.30}$$

From these matrices the interstice-interstice model mod_{ee} is built by computing the following matrices from those in Eq.23 to Eq.28:

$$\Delta_{ee_{min}}(i,j) = d_{ee_{min}}(i,j) - \frac{1}{4}\Delta d_{ee}(i,j) \quad \text{Eq.31}$$

$$\Delta_{ee_{max}}(i,j) = d_{ee_{max}}(i,j) + \frac{1}{4}\Delta d_{ee}(i,j) \quad \text{Eq.32}$$

$$\Phi_{ee_{min}}(i,j) = \phi_{ee_{min}}(i,j) - \frac{1}{4}\Delta \phi_{ee}(i,j) \quad \text{Eq.33}$$

$$\Phi_{ee_{max}}(i,j) = \phi_{ee_{max}}(i,j) + \frac{1}{4}\Delta \phi_{ee}(i,j) \quad \text{Eq.34}$$

Since they are built from a large number of imprints, models mod_{pe} and mod_{ee} contain information on the generic location of the interstices on the arch. This generic information is used to decide whether an interstice is real or not and to determine if the ordering of the interstices is coherent with the one shown in Figure 11a. To illustrate the use of these models, let us consider the example shown in Figure 12 where the label of interstice ε_v must be determined among the available labels $\varepsilon_1 \ldots \varepsilon_{15}$. Using model mod_{pe}, the constraint matrix $\Delta_{pe}(3,v)$ limits the range of possible labels for ε_v to $\varepsilon_3, \varepsilon_4, \varepsilon_5, \varepsilon_6$. In addition, the constraint matrix $\Phi_{pe}(7,v)$ limits this range to labels $\varepsilon_4, \varepsilon_5$ only. This means that labels ε_3 and ε_6 must be rejected. Model mod_{ee} can then be used to further restrict the set of admissible labels.

In practice, the interstice sets of an imprint are submitted to the constraint matrices mod_{pe} and mod_{ee}, and the interstices are labeled. For example, an initial set of interstices led to 6 possible labelings. The application of the constraint matrices allows to eliminate all but one labeling.

Figure 12 Use of models mod_{pe} and mod_{ee} for the elimination of false interstices.

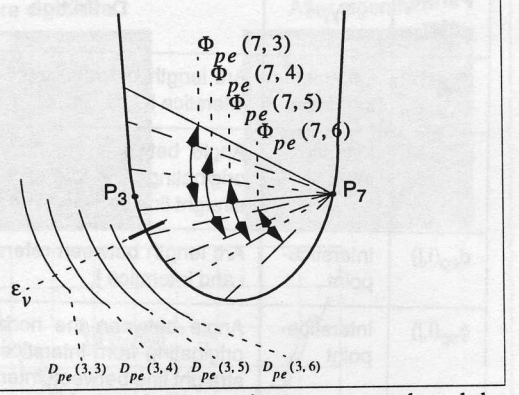

Figure 10 shows the labeled interstices on one arch and the teeth that were identified on the imprint.

3.2 Detection of feature points images of teeth

Once the interstices have been labeled correctly and the type of each tooth has been identified, the next processing step of the range images is to find feature points on each tooth.

For the extraction of feature points, the imprint is segmented into connected regions occupied by a single tooth. The area of interest inside the region is bounded by one or two interstice(s) and the lingual and buccal sides of the imprint. These regions are extracted automatically and the 3D data in the region is fitted with a cubic B-spline function in order to get an analytic description of the tooth. Details on the extraction of the regions and related processing can be found in [11].

The feature points that have to be found in order to estimate the orthodontic parameters vary with the type of tooth. For instance, the central and lateral incisors are characterized by a cutting edge at the tip of the tooth (see Figure 1). The approximate location of the ridge along the cutting edge of the incisor must be detected for the measurement of the orthodontic parameters. The most important feature point of the canine is the apex which is located at the tip of the conical shape of the tooth.

The four premolars are *bicuspids* which generally show two cusps separated by a convex ridge. The cusp with the largest depth (z-coordinate) is used for the measurement of the orthodontic parameters.

The four molars have between three to four major cusps for the maxillary arch and between three to five cusps for the mandibular arch. All cusps are needed for the measurement of the orthodontic parameters [7].

The two wisdom teeth, which are molars, are not needed for the measurement of orthodontic parameters since they are the most variable anatomically.

From the previous description of feature points on the various types of tooth, it is clear that an important processing step is to detect peaks (cusp, apex, or ridge) on the teeth. A general algorithm, called the *watershed* algorithm, has been specially designed for the detection of peaks (more precisely local minima) on a 3D surface. The *watershed* algorithm is applied to each type of tooth to find the feature points that are needed for the computation of the orthodontic parameters. This algorithm is described in detail in [11] and only the end results are shown here for canines, premolars, molars, and incisors as well as results for complete arches in Figure 13.

Figure 13 Feature points detected on two molars on a mandibular arch (a), a canine (b) on a maxillary arch, two sets of incisors on a mandibular arch (c), and two sets of incisors on a maxillary arch (d). Results for maxillary (e) and mandibular (f) arches.

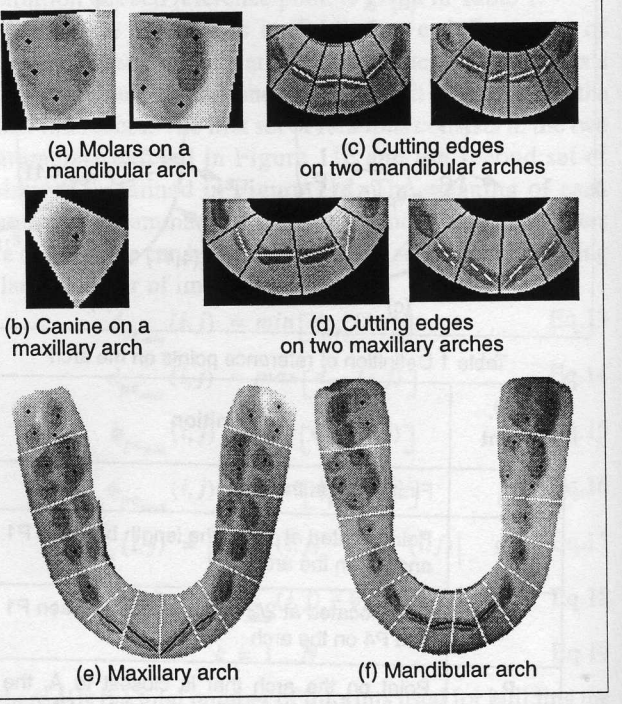

4. Conclusion and future work

A computer vision based system for the measurement of orthodontic parameters has been presented. The emphasis was put on the components of the system that are responsible for the correction of interreflections in surface concavities and for the labeling of the interstices between teeth. Experimental results are shown for a variety of cases which allow to draw the following conclusions:

1•We have noticed several problems that can affect the rate of convergence of the algorithm for the removal of interreflections:

a•Interreflected light sources outside the studied region. This is caused by the fact that, due to intensive computing time requirements, the region of interest is affected by other areas of the concave surface. This problem could be solved by a

displacement of the region of study to best cover the concave surface.

b•Interreflections during system calibration. This problem could be solved by using a minimally concave calibration part.

c•Specular reflections. A better preparation of the surface of the imprint will reduce this type of reflections.

d•Several combinations of albedo and surface orientation producing the same intensity image. This again could be solved by a better preparation of the surface prior to image acquisition.

e•Uncertainty of the effect of "estimated" occlusions on facet inter-visibility. A possible solution would be to estimate inter-visibility by using surface normals without occlusion analysis.

f•Noise in the depth image leading to more noise in the surface normals. An improvement of the sensor fusion algorithm and smoothing of the surface normals using filtering would help to reduce the noise level in surface normal estimates.

g•Acquisition system resolution. A better resolution would improve interreflection processing at the cost of increased computational load.

2•The features of interest, namely cusps and cutting edges, are detected correctly by the system. More development should concentrate on the improvement of the detection of cutting edges in order to improve the accuracy of the orientation of the edge which can have a significant effect on the measurement of the orthodontic parameters involving incisors.

3•The procedure for recording the wax imprints on subjects should be improved in order to obtain better 3D images and thus increase the performance of the processing algorithms. We have observed that several problems that occur at different processing steps could have been avoided if a better bite of the wax imprint had been recorded.

Future work will finally concentrate on the estimation of the orthodontic parameters. Finally, a clinical version of the system will have to be designed and tested. The system will be interfaced with an expert system which uses the orthodontic parameters for diagnosis.

5. Acknowledgments

This research work is supported in part by a NSERC Operating Grant. The authors are members of the Institute for Robotics and Intelligent Systems (IRIS) and wish to acknowledge the support of the Networks of Centres of Excellence Program of the Government of Canada, the Natural Sciences and Engineering Council, and the participation of PRECARN Associates Inc.

6. References

[1] L. Beaudry, "*Occlusion Indexes: A Survey*," Internal Report (in French), University of Montréal, J.-M. Brodeur Ed., Dec. 1983.

[2] C. Bernard, J.-M. Brodeur, A. Fournier, D. Poussart, D. Laurendeau, R. Guay, M. Olivier and P. Retrouvey, "Computerized Diagnosis in Orthodontics for Epidemiological Studies: A Progress Report," in *Proc. 66th Gen. Session Int. Assoc. Dental Research*, Montréal, Canada, March 9-13, 1988.

[3] J. Côté and D. Laurendeau, "A Multi-Operator Approach for the Segmentation of 3D Images of Dental Imprints," *Proc. Vision Interface*, Calgary, June 3-7, 1991, pp. 189-196.

[4] D. Forsyth and A. Zisserman, "Reflections on Shading", *IEEE Transactions on Pattern Analysis and Machine Intelligence*, Vol. 13, No. 7, July 1991, pp. 671-679.

[5] D. Forsyth and A. Zisserman, "Mutual Illumination", *Proceedings Computer Vision and Pattern Recognition '89*, IEEE Computer Society Press, Los Alamitos CA, 1993, pp. 466-473.

[6] D. Forsyth and A. Zisserman, "Shape from shading in the light of mutual illumination", *Image and Vision Computing*, Vol. 1, No. 1, Feb. 1983, pp. 671-679.

[7] B.S. Kraus, R.E. Jordan and L. Abrams, "*A Study of the Masticatory System Dental, Anatomy and Occlusion*," B.C. Decker, Toronto, Canada, 1988.

[8] S.K. Nayar, X. Fang and T. Boult, "Removal of Specularities Using Color and Polarization", *Proceedings Computer Vision and Pattern Recognition '93*, IEEE Computer Society Press, Los Alamitos CA, 1993, pp. 583-590.

[9] S.K. Nayar, K. Ikeuchi and T. Kanade, "Shape from Interreflections", *Proceedings Third International Conference on Computer Vision*, IEEE Computer Society Press, Los Alamitos CA, 1990, pp. 2-11.

[10] F. Méthot, M. Mokhtari, D. Laurendeau and D. Poussart, "Sensor fusion of 2D and 3D Data for the Processing of Images of Dental Imprints", *Proc. SPIE Conf. on Algorithms and Techniques*, Vol 2055, Boston, Mass., Sept. 7-10, 1993.

[11] M. Mokhtari and D. Laurendeau, "Feature Detection on 3D Images of Dental Imprints, *CVPR Proc IEEE Workshop on Biomedical Image Analysis*, Seattle, WA, June 1994.

[12] R. Wolfe, "*Modelling of the interreflections for a Range Finder Based on the Differential Absorption of Light*", Master's Thesis, Department of Electical and Computer Engineering, Laval University, 1996 (In French).